All-Solid-State Batteries

How to cite: *Angew. Chem. Int. Ed.* **2023,** *62,* e202302363
International Edition: doi.org/10.1002/anie.202302363
German Edition: doi.org/10.1002/ange.202302363

Understanding Electrochemical Reaction Mechanisms of Sulfur in All-Solid-State Batteries through Operando and Theoretical Studies **

Daxian Cao[+], Xiao Sun[+], Fei Li[+], Seong-Min Bak, Tongtai Ji, Michael Geiwitz, Kenneth S. Burch, Yonghua Du, Guochun Yang, and Hongli Zhu**

Abstract: Due to its outstanding safety and high energy density, all-solid-state lithium-sulfur batteries (ASLSBs) are considered as a potential future energy storage technology. The electrochemical reaction pathway in ASLSBs with inorganic solid-state electrolytes is different from Li-S batteries with liquid electrolytes, but the mechanism remains unclear. By combining operando Raman spectroscopy and ex situ X-ray absorption spectroscopy, we investigated the reaction mechanism of sulfur (S_8) in ASLSBs. Our results revealed that no Li_2S_8, Li_2S_6, and Li_2S_4 were formed, yet Li_2S_2 was detected. Furthermore, first-principles structural calculations were employed to disclose the formation energy of solid state Li_2S_n ($1 \le n \le 8$), in which Li_2S_2 was a metastable phase, consistent with experimental observations. Meanwhile, partial S_8 and Li_2S_2 remained at the full lithiation stage, suggesting incomplete reaction due to sluggish reaction kinetics in ASLSBs.

[*] D. Cao,[+] X. Sun,[+] T. Ji, H. Zhu
Department of Mechanical and Industrial Engineering, Northeastern University
360 Huntington Avenue, Boston, MA 02115 (USA)
E-mail: h.zhu@neu.edu

F. Li,[+] G. Yang
State Key Laboratory of Metastable Materials Science & Technology and Key Laboratory for Microstructural Material Physics of Hebei Province, School of Science, Yanshan University
Qinhuangdao 066004 (China)
E-mail: yanggc468@nenu.edu.cn

S.-M. Bak, Y. Du
National Synchrotron Light Source II, Brookhaven National Laboratory
Upton, NY 11973 (USA)

M. Geiwitz, K. S. Burch
Department of Physics, Boston College
140 Commonwealth Ave, Chestnut Hill, MA 02467-3804 (USA)

[+] These authors contributed equally to this work.

[**] A previous version of this manuscript has been deposited on a preprint server (https://doi.org/10.26434/chemrxiv-2022-vk5lb).

Introduction

Lithium-sulfur (Li-S) batteries have attracted extensive attention because of their ultrahigh theoretical energy density (2600 $Wh\,kg^{-1}$), almost ten times higher than current commercial lithium-ion batteries.[1] However, conventional Li-S batteries with ether-based liquid electrolytes (LEs) experience rapid capacity decay, low coulombic efficiency, and poor cycling life, mainly caused by the shuttle effect, i.e., the formation and movement of highly soluble long-chain polysulfide intermediates (Li_2S_n, $4 \le n \le 8$).[2] Moreover, the combustible organic LEs pose a risk to the batteries' safety. All-solid-state Li-S batteries (ASLSBs) that replace the traditional organic LEs with inorganic solid-state electrolytes (SEs) are proposed to fundamentally solve the aforementioned issues. Inorganic SEs are not combustible, thus avoiding thermal runaway of the batteries, and their use prevents the development of soluble polysulfides, which can solve the shuttle effects.[3] Among different SEs, sulfide SEs own remarkable processability and ionic conductivity ($>10\,mS\,cm^{-1}$), which is comparable with LEs.[4] However, the performance of the ASLSBs is still far from expectations, especially the rate performance is much lower than in LEs. The underlying reaction mechanisms of sulfur cathode (S_8) in the ASLSBs haven't been fully understood yet. More fundamental investigations are highly desired.

The overall electrochemical reaction during charge and discharge, regardless of whether they are using LEs or SEs, is represented by Equation (1):

$$S_8 + 16Li^+ + 16e^- \leftrightarrow 8Li_2S \quad (1)$$

The reaction mechanisms and intermediate chemistries in liquid Li-S batteries have been extensively investigated.[5] Upon galvanostatic discharge, two plateaus are observed, corresponding to the generation of soluble long-chain (Li_2S_n, $4 \le n \le 8$) and solid short-chain (Li_2S_2) polysulfide intermediates. In comparison, the inorganic SEs-based ASLSBs show different charge/discharge behaviors. The charge and discharge curves in ASLSBs exhibit only one pair of plateaus. The single plateau is generally taken as an indication of a direct reaction between S_8 and Li_2S with no intermediates formed. Another explanation is that the lack of solvation in SEs prevents the formation of long-chain polysulfides.[6] However, there has been no clear evidence to prove whether Li_2S_2 is present in the ASLSBs or not. Li_2S_2, as a short-chain

polysulfide, is insoluble in LEs, thus it should not be affected by the solvation issue. In addition, since S_8 and Li_2S are both criticized for their insulating properties, the conversion between them is challenged by the reaction kinetics. The conversion from S_8 to Li_2S_2 contributes half of the total theoretical capacity, and the polysulfide intermediates are reported to alleviate kinetic limitations.[7] Therefore, the existence of Li_2S_2 may affect the performance of ASLSBs greatly. Hence it is significant to identify the reaction mechanisms in ASLSBs, thus advanced characterizations are required.

Operando investigation can provide real-time information during electrochemical reactions, which is important for a fundamental understanding of ASLSBs.[8] However, it is also challenging due to the complex operating requirements and special cell designs. For example, sulfide SEs are highly sensitive to the ambient environment, especially the moisture in the air.[9] Ensuring proper sealing is essential, but the sealing material impedes the collection of signals or detectability. Meanwhile, the sulfide SEs-based ASLSBs are generally operated under a high stacking pressure.[10] Therefore, a specially designed in operando pressurized cell is desired to maintain high stacking pressure during the characterization. In comparison, ex situ characterizations are easier to conduct in sample preparation and measuring conditions but face the challenges of discontinuity, contamination, and distraction information.[11] By combining in operando investigation and ex situ characterization, a balance between accuracy and feasibility can be achieved, thus providing a comprehensive understanding of the reactions in ASLSBs.

Herein, for the first time, we investigated the chemistries evolution of the cathode in sulfide SEs-based ASLSBs and revealed the reaction mechanism by combining operando Raman spectroscopy, ex situ synchrotron X-ray absorption spectroscopy (XAS), and first-principles calculations. We designed a dedicated cell that can be operated with a high stacking pressure and successfully conducted the operando Raman spectroscopy using our cleanroom in a glovebox [12]. The chemistries evolution of sulfur element is recorded in real-time. Meanwhile, ex-situ XAS was employed to accurately identify the chemistries in the cathode at different depths of discharge (DoD) and states of charge (SoC). Through the first-principles calculations, the reaction processes of S_8 in ASLSBs are further elucidated, and the sluggish reaction kinetic in ASLSBs is also discussed. This work pioneers the investigation of the fundamental reaction mechanism of S_8 in ASLSBs, offering a basis for the design of high-performance ASLSBs.

Results and Discussion

The electrochemical reaction processes are significantly different in the Li-S batteries using LEs and SEs. Figure 1a illustrates the electrochemical reaction process of S_8 in the conventional Li-S battery using ether-based LEs.[13] During the discharge process, S_8 is subsequently reduced to soluble long-chain lithium polysulfides with a gradual decrease in the chain length.[14] Then the long-chain polysulfides are further reduced to insoluble Li_2S_2, corresponding to a liquid-solid dual phase conversion. Finally, Li_2S_2 is reduced to the final product, Li_2S. Due to the sluggish solid-solid reaction kinetic, the theoretical capacity is hard to obtain, thus the final reduction product in the real battery is generally a mixture of Li_2S_2 and Li_2S instead of the desired pure Li_2S.[15] During the charging process, Li_2S_2 and Li_2S react in a two-phase reaction process, generating polysulfide intermediates and eventually converting back to solid S_8.[16] The shuttle effect of soluble long-chain lithium polysulfides is one of the most critical problems that reduce the electrochemical performance of liquid Li-S batteries, which has been widely investigated.

In comparison, till now, the exact chemistry evolution and reaction mechanism in ASLSBs are still unclear, as depicted in Figure 1b. There are still many unanswered questions related to the ASLSBs: What is the reason for the lack of two plateaus in the galvanostatic discharge of ASLSBs? Are there any intermediates generated in the transformation from S_8 to Li_2S? How will these intermediates affect the battery′s performance? How is the "shuttle effect" inhibited by the SE? Answers to these questions are significant in understanding the mechanism of ASLSBs. Advanced characterizations are highly desired for a deep understanding.

Raman spectroscopy is a powerful tool because it can determine the molecules via lattice modes and function group vibrational frequencies. Operando Raman spectroscopy has been widely used in investigating the reaction mechanism of S_8 in batteries using LEs,[11] but its application in ASLSBs is scarce. One challenge is the sample signals during the operando test may be weakened by the sealing material, such as glass or quartz window, since the cell sealing is desired in a conventional Raman test for ASLSBs, especially for air-sensitive sulfide SEs. Meanwhile, since the ASLSB generally works under a high pressure, the cell should have the capability to be applied the desired pressure. Therefore, we designed an operando Raman test as shown in Figure 1c. This operando test was carried out in a "cleanroom-in-a-glovebox system",[12] in which the Raman is placed inside an argon environment. The system allows the characterization of ASLSBs in an inert argon atmosphere with no sealing needed. The cell was designed with a side opening, enabling the inside material to be directly exposed to the laser, thereby avoiding any Raman signal losses caused by the window material. More important, a stainless-steel framework was employed to manage the pressure within the ASLSBs, ensuring that the electrochemical reaction is accurate to provide a basis for operando measurements. The opening is designed in a square shape to ensure the laser beam can be precisely focused on a flat sample surface, thereby eliminating the signal degradation or unwanted scattering. The cathode, SE, and anode were layer-by-layer stacked together into a pallet in a cuboid polyether ether ketone (PEEK)-made die and a high stacking pressure can be maintained with the stainless-steel framework during the test. Figure S1 shows photographs of the ASLSB cell designed for this study and the correspond-

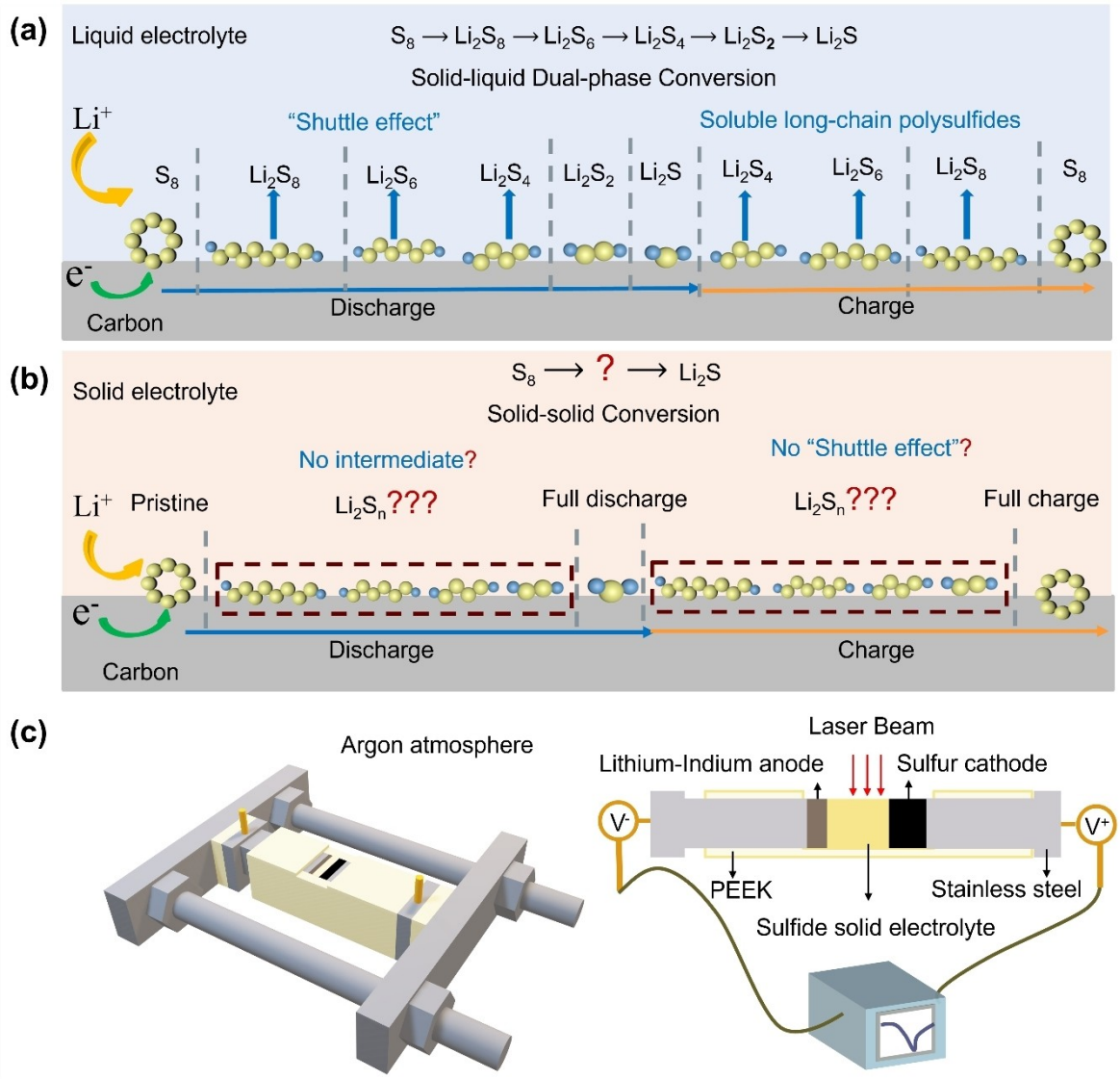

Figure 1. Electrochemical reaction mechanisms of S_8 in a) liquid electrolyte and b) solid electrolyte. c) Schematic illustration of the specially designed cell for operando Raman spectroscopy ASLSB test and the components of the setup.

ing Raman spectroscopy setup. During the Raman test, we can observe the cross-section of ASLSBs with an optical microscope inside the glovebox, as depicted in Figure S2, and the thickness of the cathode is estimated to be around 26 μm.

Li-S batteries using liquid and solid electrolytes exhibit different charge/discharge profiles, indicating different electrochemical pathways of S_8. Figures 2a and b illustrate the galvanostatic charge/discharge profiles of solid and liquid cells in the initial cycle at a current rate of 0.1 C, which is calculated based on a theoretical capacity of 1675 mA g^{-1} at 1 C. As shown in Figure 2a, the solid cell shows only one pair of plateaus and delivers initial discharge and charge capacities of 1167 and 1014 mAh g^{-1}, separately. In comparison, the liquid cell shows two plateaus during the initial discharge and one plateau in the charging process, as shown in Figure 2b. The initial discharge and charge capacities are 1139 and 993 mAh g^{-1}, respectively. The distinction between the two profiles is due to different fundamental reaction pathways. The two plateaus of the liquid cell can be attributed to the liquid-solid two-phase transformation. The upper discharge plateau is assigned to the solid-to-liquid conversions from S_8 to Li_2S_8, Li_2S_6, and Li_2S_4.[13,17] The lower discharge plateau is attributed to the liquid-to-solid conversions from Li_2S_4 to Li_2S_2 and Li_2S. During the charging process, there is only one plateau attributed to the conversion from short-chain polysulfides to long-chain polysulfides.[5a] In comparison to these well-known processes in the liquid cell, the mechanism in the solid cell has never been well discussed.

The potential values in both solid and liquid cells at 50 % of the DoD and the SoC are utilized to evaluate the reaction kinetics. The voltage gap of the solid cell is 640 mV (2.44 V at 50 % of SoC and 1.80 V at 50 % DoD). In

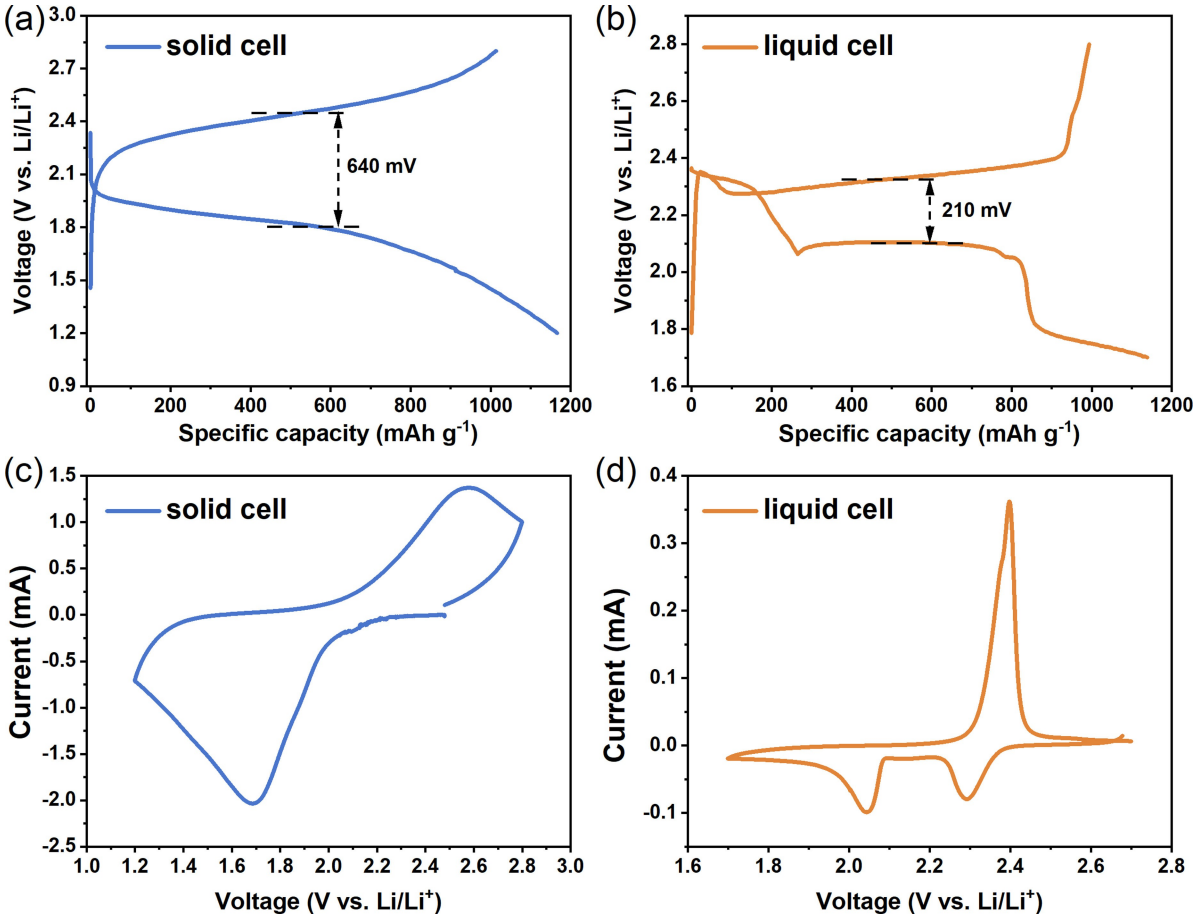

Figure 2. Electrochemical behavior comparison between solid cell and liquid cell. Galvanostatic charge/discharge profiles of a) solid cell and b) liquid cell at the rate of C/10 at the first cycle. CV profile of c) solid cell and d) liquid cell at a scan rate of 0.1 mV s^{-1} at the first cycle.

comparison, the voltage gap of the liquid cell is 210 mV (2.31 V at 50 % of SoC and 2.10 V at 50 % DoD), which is 430 mV smaller than the solid cell. The voltage gap in the solid cell being three times larger than that of the liquid cell indicates a slower reaction kinetic, which is attributed to slower charge transfer, point-to-point ion diffusion at the interface, and a larger conversion energy in the solid-solid reaction.

Figures 2c and d compare the cyclic voltammetry (CV) curves of the solid cell and liquid cell at the scan rate of 0.1 mV s^{-1}. In the solid cell, there is one pair of broad reduction and oxidation peaks at 1.69 and 2.56 V. In comparison, in the liquid cell, two reduction peaks exist at 2.29 and 2.04 V in the cathodic scan, and one oxidation peak at approximately 2.40 V in the anodic scan. The distribution of CV peaks agree well with the galvanostatic charge and discharge profiles in Figures 2a and b.

Operando Raman spectroscopy was conducted to reveal the chemistries and reaction mechanisms in ASLSBs. Figures 3a–c show the Raman spectra of SE and cathode before cycling. As shown in Figure 3a, SE has one dominant Raman peak at 427 cm^{-1}, which can be attributed to the PS_4^{3-} structural unit in the argyrodite-type SE.[18] As to the cathode, we measured the Raman spectra of two different positions, labeled as positions A and B (Figure S3), as a pristine reference. As shown in Figures 3b and c, at both positions A and B, three obvious Raman peaks at 158, 220, and 473 cm^{-1} are observed, which belong to the active material S_8.[19] Since the cathode is a mixture of S_8, SE, and carbon additive, another two peaks observed at 176 and 310 cm^{-1} are assigned to the stretching and in-plane bending of the C–S bond, respectively (Figure S4).[20] This bond is formed in the thermal treatment process after mixing. However, only position A has the Raman peaks belonging to the SE.

Figure 3d displays the voltage-time profile of ASLSB (left side) and the Raman spectra at Position B in the operando test (right side). The voltage profile shows only one pair of plateaus when tested between 1.2 and 2.8 V at 0.1 C. The Raman intensity mapping presents the real-time evolution of the chemicals. During the discharging process, the intensity of the peaks belonging to S_8 (158, 220, and 473 cm^{-1}) becomes weak but persists even in the full discharge state. This shows the gradual reduction process of S_8 and the conversion is not thoroughly conducted. No obvious new peak presents during the discharging process. In comparison, during the charging process, there is a newborn peak at ≈438 cm^{-1}, besides the increase of

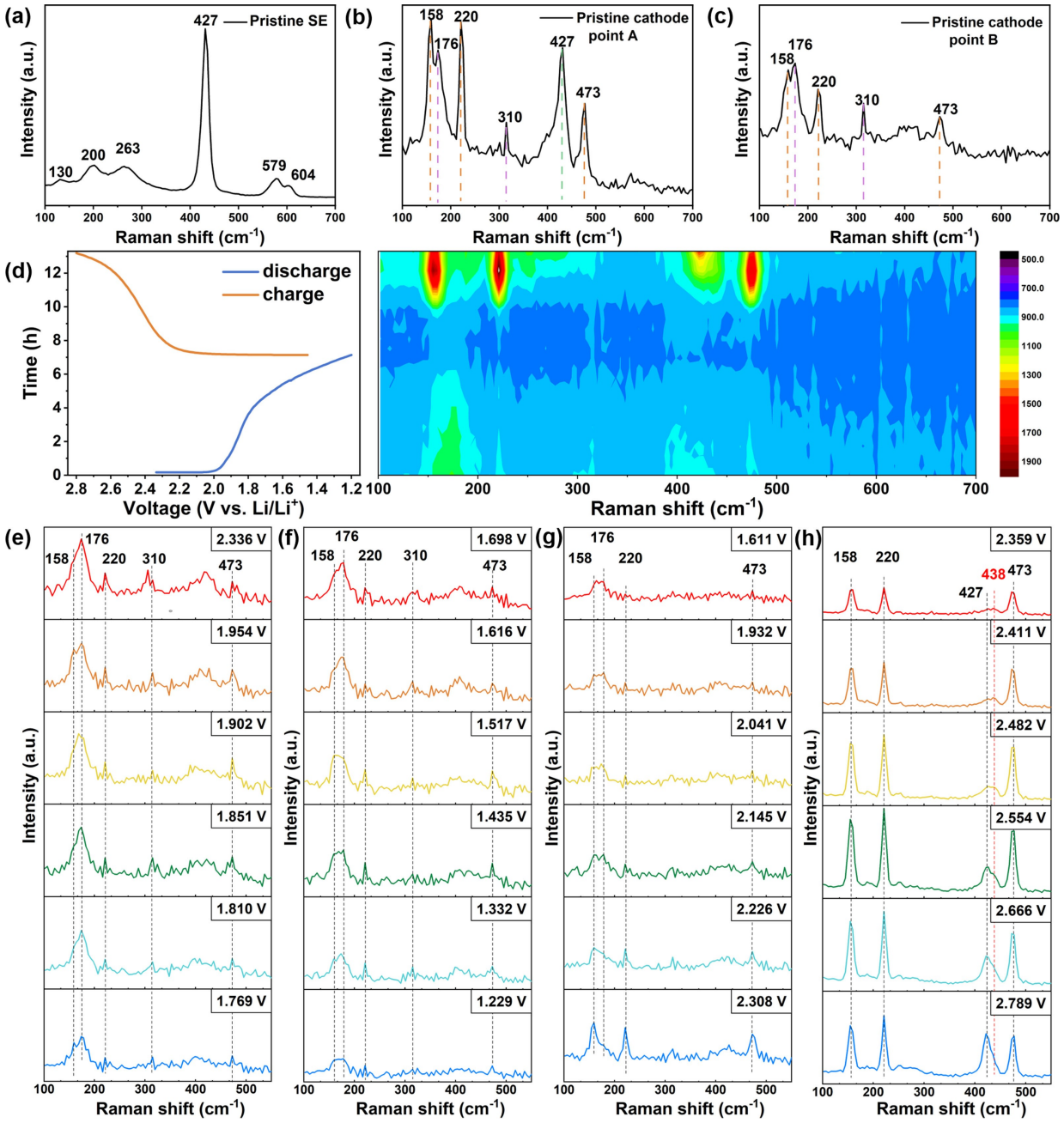

Figure 3. Operando Raman investigation. Raman spectra of a) the SE and b), c) cathode at two different positions before cycling. d) Time-voltage profile of the ASLSB and the corresponding real-time Raman intensity mapping in the operando test. Operando Raman spectra of ASLSBs at various voltage during e)–f) the discharge and g)–h) charge process.

intensities of S_8 peaks. This suggests that there are new chemicals formed when the reduction product recovers to S_8 during the oxidation process, indicating a stable electrochemical reaction. The specific new chemicals will be further identified in the following.

For a more detailed investigation, we selected the spectra at different discharge and charge states. As shown in Figures 3e and f, the Raman intensities of three characteristic S_8 peaks (158, 220, and 473 cm^{-1}) decrease gradually when the cell is discharged. The Raman intensity of the C–S bond (176 and 310 cm^{-1}) also slightly decreases. At the final discharge state (1.229 V), not all S_8 peaks disappear, demonstrating that the electrochemical reaction of S_8 is insufficient in ASLSBs. Figures 3g and h show the spectra during the charging process. Peaks belonging to S_8 become stronger as the voltage increases. The peaks belonging to the C–S bond are not recovered, demonstrating the enhanced S_8 peak is attributed to the electrochemical reactions. More importantly, there is a newborn peak at 438 cm^{-1} that appears at the half charge state (2.359 V in Figure 3h). This peak gradually rises and disappears at a full charge state (2.789 V in Figure 3h), which can be attributed

to the Li_2S_2.[21] However, due to the relatively small percentage of Li_2S_2 in the whole composite electrode, the peak intensity is low. No other polysulfides are observed during the charging and discharging processes. This demonstrates that the Li_2S is oxidized to Li_2S_2 first and then converts to S_8 in the charging process. In addition, it is interesting that the peak of SE gradually appears in the charging process, indicating that the SE is exposed to the laser with the volume shrinkage of cathode material due to the conversion from Li_2S to S_8.

Synchrotron XAS at the sulfur K-edge was employed to gain further insight into the electrochemical chemistries of the cathode in the ASLSBs, due to its high sensitivity to the sulfur element chemical state. Since the sulfide SE is reported with a redox reaction behavior in ASLSBs, we investigated its stability in a control cell first to confirm that the sulfur element chemical status revolution is all derived from the S_8 rather than the sulfide SE. The control cell with a cathode composed of SE and carbon additive in a weight ratio of 1:5 was operated at the same voltage range as the ASLSBs. Figure 4a displays the sulfur K-edge X-ray absorption near edge structure (XANES) spectra of the control cathode in pristine, full discharge, and full charge states. At the near edge region, all three spectra show the same features at 2472.1, 2473.7, and 2477.7 eV assigned to the SE, suggesting that the SE is quite electrochemically stable within the working potential from 1.2 to 2.8 V (vs. Li/Li^+). Thus, we can determine that the chemical state alteration of the sulfur element in ASLSBs is ascribed to the active material, not SE.

Figure 4b shows the sulfur K-edge XANES of the cathode in the ASLSB at different discharge states. Pure S_8 and Li_2S were investigated as standard references: S_8 has two features at 2473.0 and 2480.0 eV; Li_2S shows three peaks at 2474.0, 2476.7, and 2484.3 eV. The spectrum of the pristine cathode has one peak at 2473.0 and a fine structure of 2480.0 eV assigned to the S_8. The linear combination fitting (LCF) figure of the XANES spectrum (Figure S5) confirms the pristine cathode is the mixture of SE and S_8 before cycling. When the cathode is discharged to 1.8 V (labeled as half discharge), the feature at 2480 eV shifts to 2478 eV, while the main peak of 2473 eV remains with the development of the shoulder at near 2471.3 eV, as highlighted in Figures 4c and d. This feature is associated with the short-chain polysulfide, Li_2S_2.[5b] When the cathode reaches a full discharge state at 1.2 V, there are four features at 2472.1, 2474.0, 2476.7, and 2484.3 eV, which implies a complex nature. To further determine the components at this stage, firstly, we performed LCF analysis using Li_2S, S_8, and SE for the XANES spectrum at the full discharge state (Figure S6). Most features are matched, except a shoulder with energy below 2472.1 eV which is similar to the half discharge state. Therefore, we concluded the full discharge composition as the S_8, Li_2S, SE, and Li_2S_2. Overall, during the discharge process, the cathode active material undergoes a transition from S_8 to Li_2S accompanied by forming an intermediate phase, Li_2S_2, while no long-chain polysulfides are formed. In addition, due to the sluggish reaction kinetics, some S_8 still exist at the full discharge state.

When the cathode is charged back to 2.4 V (half charged state), the XANES spectrum appears the same as the half-discharged state, indicating that partial Li_2S is converted to Li_2S_2, as highlighted in Figures 4c and d. At the full charge state of 2.8 V, peaks belonging to Li_2S_2 partially disappear, all Li_2S peaks disappear, and two features of S_8 are back, suggesting the conversion from Li_2S and Li_2S_2 to S_8 occurs (Figure S7). Similarly, no bulky Li_2S_n ($4 \leq n \leq 8$) are observed in this process. In short, during the charging process, the Li_2S is first oxidized to Li_2S_2 and finally transformed to S_8. The successful recovery from Li_2S to S_8 suggests notable reversibility in the ASLSBs. The cathode chemistries at the half charge state after 40 cycles were investigated, as shown in Figure 4se and f. Increased intensity of the shoulder peak at 2471.3 eV is observed, implying an accumulation of Li_2S_2 intermediate species due to sluggish reaction kinetics in ASLSB in long-term cycling.

We try to further unveil the reaction mechanism of ASLSBs from the standpoint of first-principles calculations. Based on the above results, it is clear that the reaction pathway in ASLSBs is distinct from that of Li-S batteries using the liquid electrolyte. To fundamentally understand the discharge/charge processes in ASLSBs, we need to know the crystal structures of Li_2S_8, Li_2S_6, Li_2S_4, Li_2S_2, and Li_2S (Table S1), and then employ them to estimate the relative stabilities and determine the discharge products based on the calculated formation energy (Table S2) and construct convex hull, respectively. Generally, the phases lying on the convex hull are stable against decomposition into any other binary compositions and elemental solids. The structures sitting on the dotted lines are either unstable or metastable (assuming their phonon dispersion curves are real), and they will either decompose into other stable compounds or elemental solids or are in metastable states if the kinetic barriers are high.[22] For the latter case, those structures have a large possibility to be formed if their formation energies are less than 50 meV.[23]

Thus far, first-principles structural search technology can effectively disclose ground-state structure that only depends on the given chemical composition,[24] which has played an irreplaceable role in accelerating the discovery of new materials and understanding the chemical reaction.[25] Here we carry out an extensive structural search with the above-mentioned Li_xS_y compositions through swarm-intelligence structural search calculations.[24d,26] The experimentally known anti-fluorite structure of Li_2S is readily identified in our structural search, and the optimized lattice constant of 5.71 Å is in good agreement with the measured 5.69 Å.[27] This indicates that our adopted structural search technology and pseudopotentials are suitable for the Li-S system. Subsequently, we estimate their relatively thermodynamic stabilities based on the constructed convex hull (Figure 5a). Li_2S is the only stable chemical composition. The formation energies (e.g., 304.0, 63.8, and 63.6 meV/atom) of Li_2S_8, Li_2S_6, and Li_2S_4 are much higher than 50 meV/atom. They also present obvious imaginary frequencies in the phonon spectra (Figure S8). These features preclude their existence as the final discharge products. For the Li_2S_2 with a $P4_2/mnm$ symmetry, its formation energy is 48.5 meV/atom, and

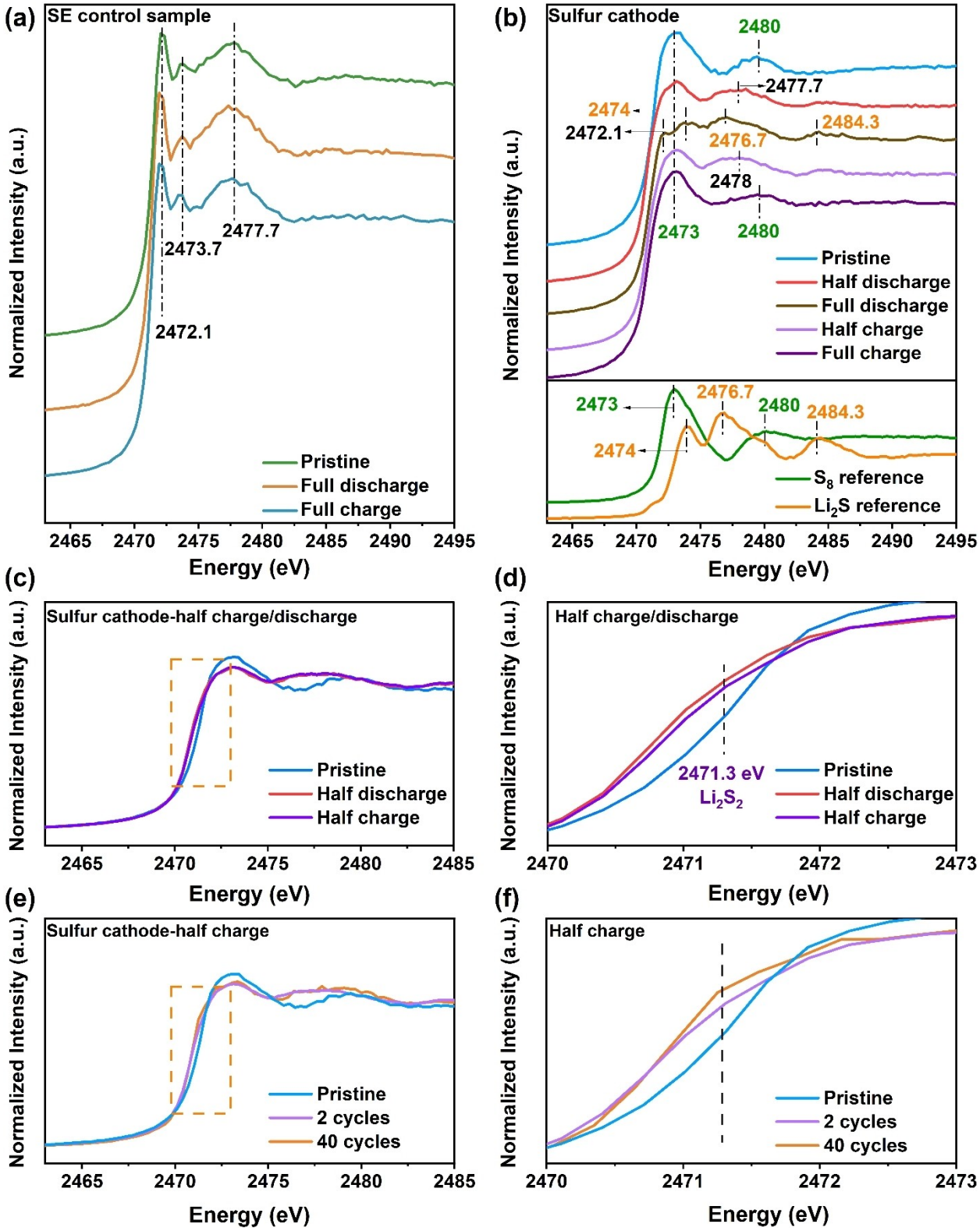

Figure 4. Understanding the reaction mechanism of ASLSBs through ex situ sulfur K-edge XANES. XANES profiles of a) SE control sample and b) cathode in different charge/discharge states and references. c) XANES profiles comparison of the cathode in pristine, half charge, and half discharge states. d) The zoom-in spectra show the feature of Li_2S_2 in (c). e) XANES profiles comparison of the cathode in a pristine state, half charge states after 2 cycles and 40 cycles. f) The zoom-in spectra show the feature of Li_2S_2 in (e).

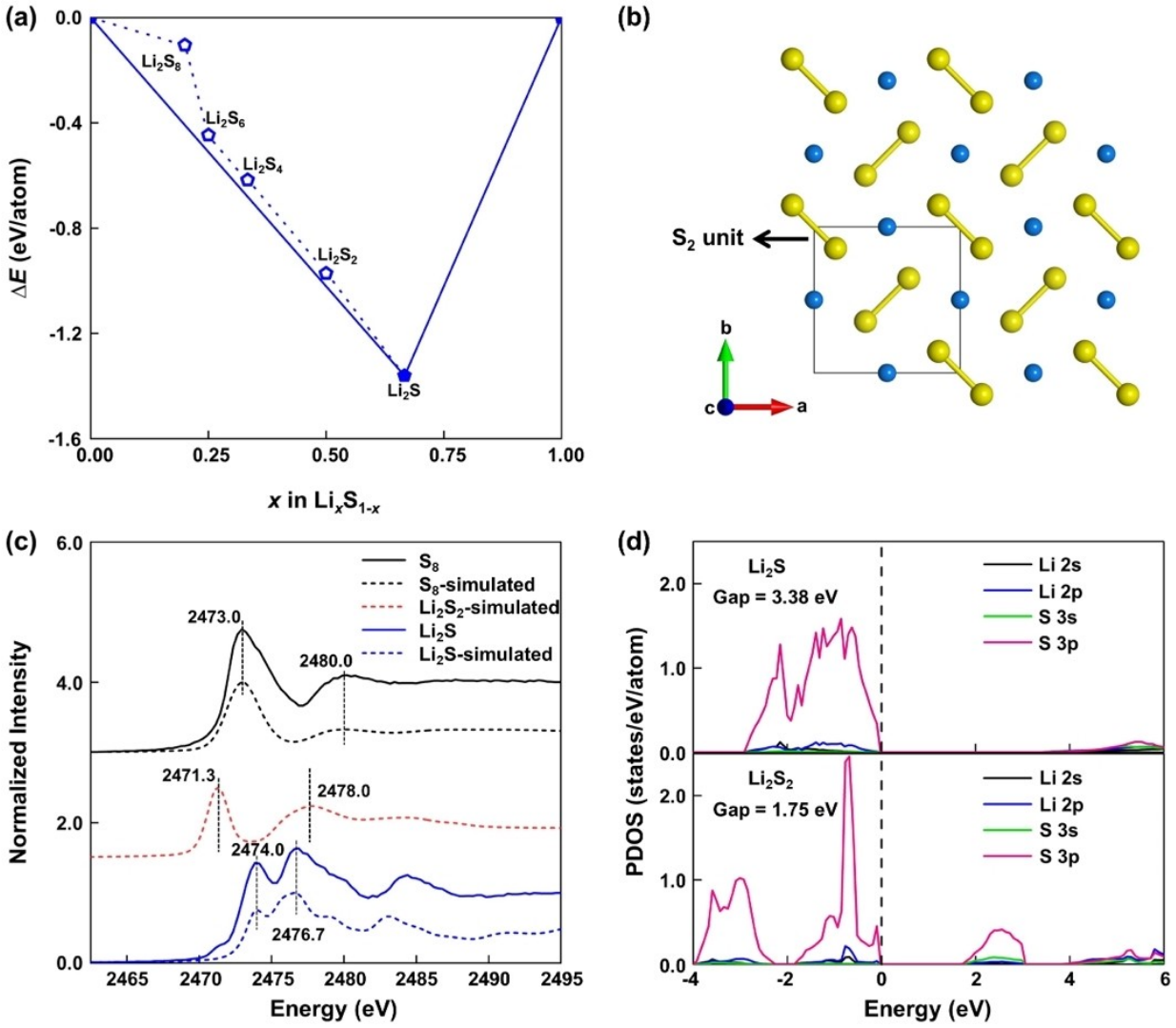

Figure 5. First-principles calculation. a) Formation energy with respect to solid Li and S for the various Li-S compounds at 0 GPa. A body-centered cubic (bcc) structure of elemental Li[24e] and the α-phase of S[29] are used to calculate the formation energy of each Li-S binary composition. The convex hulls are shown by solid lines. b) The S_2 units in $P4_2/mnm$ Li_2S_2 are perpendicular to each other along *ab* plane. c) The comparison between measured and simulated sulfur K-edge XANES spectra of S_8 and Li_2S, along with the simulated ones of Li_2S_2. d) The density of states of Li_2S_2 and Li_2S at the PBE level of theory. In general, the smaller the band gap, the larger the intrinsic charge carriers.

is dynamically stable (absence of imaginary modes, Figure S8), meeting the requirement of a metastable phase. On the other hand, Li_2S_2 is also mechanically stable (Table S3). The striking feature of Li_2S_2 is that it consists of quasimolecular S_2 units (Figure 5b) that are perpendicular to each other.[28]

Subsequently, we explore the possibility of our proposed Li_2S_2 as the final discharge product from the standpoint of thermal stability, discharge profile, K-edge XANES spectra, and density. After the molecular dynamics simulations at the temperatures of 300 and 500 K, there appears slight structural deformation, but no bond breaking (Figure S9), indicating that our proposed Li_2S_2 has excellent thermal stability. For the conversion of $S_8 + 8Li^+ + 8e^- \rightarrow 4Li_2S_2$, the calculated voltage platform of 1.94 V is comparable to the measured 1.80 V (half discharge). In addition, we try to obtain more information from sulfur K-edge XANES spectra (Figure 5c), which is sensitive to the local chemical environment. The measured K-edge XANES spectra of S_8 and Li_2S are well reproduced by our simulations (Figure 5c). What is the correlation between the proposed Li_2S_2 and the measured one? In the half discharge process, the two main peaks of 2473 and 2480 eV of S_8 shift to 2471.3 and 2478 eV, which perfectly match with the simulated 2471.3 and 2478 eV of Li_2S_2 (Figure 5c). At full discharge state (Figures 4a and b), the measured first peak of 2472.1 eV can be assigned to the main peak of 2471.3 eV in Li_2S_2. The other three peaks are attributed to those of Li_2S. Finally, the density of 1.65 $g\,cm^{-3}$ of the predicted Li_2S_2 is comparable to 1.66 $g\,cm^{-3}$ of Li_2S, which does not rule out the possibility of coprecipitation. Finally, the calculated electron band gap (1.75 eV) of Li_2S_2 is much smaller than the 3.38 eV of Li_2S

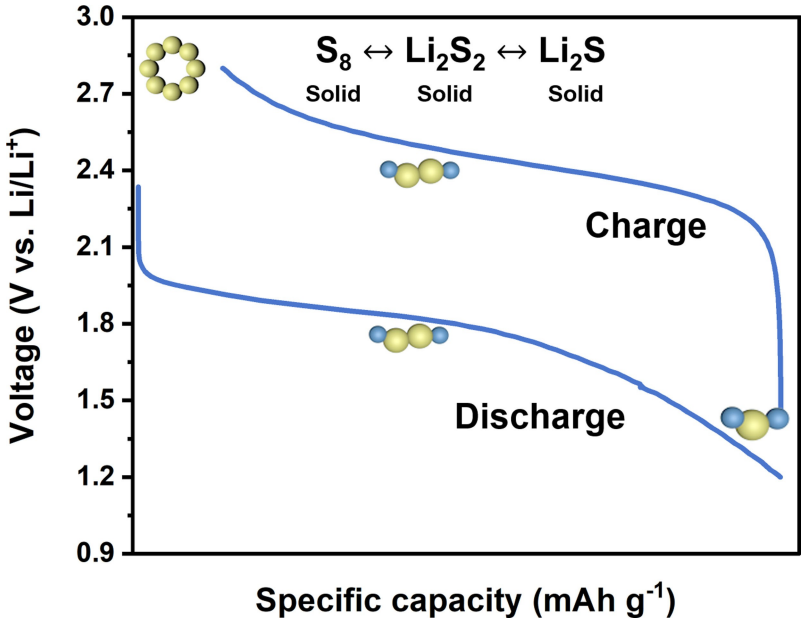

Figure 6. The typical charge/discharge profile of ASLSBs. The inset schematic illustrates the reaction mechanism.

(Figure 5d), which means that Li_2S_2 is more electrically conductive than Li_2S, benefiting the electrochemical reaction kinetic.

In conclusion, as illustrated in Figure 6, the electrochemical redox reactions in the ASLSB are conversions between the S_8 and Li_2S with an intermediate phase of Li_2S_2 formation, but no Li_2S_8, Li_2S_6 and Li_2S_4 present. The S_8 firstly transfers to the Li_2S_2 [Eq. (2)], then it further reduce to the final product Li_2S [Eq. (3)] during the discharging process. During the charging process, these reactions reverse.

$$S_8 + 8Li^+ + 8e^- \leftrightarrow 4Li_2S_2 \quad (2)$$

$$4Li_2S_2 + 8Li^+ + 8e^- \leftrightarrow 8Li_2S \quad (3)$$

The solid-solid reduction process is kinetically slow, leading to the premature termination of the discharge product. In addition, the utilization of S_8 in SE is limited due to lacking efficient ion and electron conductivity and sluggish reaction kinetics. In consequence, the full discharge product is a mixture of Li_2S, Li_2S_2, and unreacted S_8. During the charging process, Li_2S converts back to Li_2S_2 first and then to S_8, resulting in a reversible reaction, whereas a certain amount of Li_2S_2 can't be fully oxidized to S_8 due to the sluggish reaction kinetics. At the same time, no long-chain polysulfides are generated during the whole process, which is intrinsically different from in LEs, indicating the elimination of the "shuttle effect" in ceramic SE.

Conclusion

In summary, we comprehensively investigated the reaction mechanisms of the sulfur cathode (S_8) in the all-solid-state lithium-sulfur batteries (ASLSBs) through the operando Raman spectroscopy and ex-situ X-ray absorption near edge structure (XANES). A particular operando Raman investigation is designed to exclude the potential complications caused by the operating atmosphere and pressure issues through "cleanroom-in-a-glovebox system" and unique cell design. For the first time, we revealed the electrochemical redox reactions in ASLSBs are solid-solid conversions between the S_8 and Li_2S with an intermediate phase Li_2S_2 formation. No polysulfides Li_2S_8, Li_2S_6, and Li_2S_4, are found, which matches with one discharge plateau in ASLSB in comparison to the two discharge plateaus in liquid cells. The First-principles calculations demonstrate that Li_2S_2 is a metastable phase that can be synthesized at solid conditions, whereas bulky Li_2S_4, Li_2S_6, and Li_2S_8 are unstable from the standpoint of thermodynamics and dynamics. The transitions among S_8, Li_2S_2, and Li_2S show sluggish reaction kinetics in ASLSBs due to the solid-solid conversions and slow charge transfer, which results in the insufficient utilization of S_8 in the ASLSBs. Therefore, finding strategies to accelerate the sluggish solid-solid conversion is critical in developing high-performance ASLSBs. In addition, sulfide solid electrolyte shows remarkable electrochemical stability at the voltage range from 1.2 to 2.8 V (vs. Li/Li^+), which benefits battery stability. Through comprehensive analysis, we identified the specific chemistries in ASLSBs during different charge/discharge states and explored a clear electrochemical reaction pathway in the cathode.

Acknowledgements

H.Z. acknowledge the financial support from National Science Foundation under Award Number CBET-ES-1924534. The authors also acknowledge the 8-BM of the

National Synchrotron Light Source II, a U.S. Department of Energy (DOE) Office of Science User Facility operated for the DOE Office of Science by Brookhaven National Laboratory under Contract No. DE-SC0012704. This research used 8-BM of the National Synchrotron Light Source II, a U.S. Department of Energy (DOE) Office of Science User Facility operated for the DOE Office of Science by Brookhaven National Laboratory under Contract No. DE-SC0012704. M.G. and K.S.B. are grateful for the support of the National Science Foundation (NSF) EPMD program via grant 2211334. The authors acknowledge Prof. Yue Qi from Brown University for meeting and discussion.

Conflict of Interest

The authors declare no competing financial interest.

Data Availability Statement

Research data are not shared.

Keywords: All-Solid-State Lithium-Sulfur Batteries · Operando Raman Spectroscopy · Solid-State Reactions · Sulfur · X-Ray Absorption Spectroscopy

[1] a) R. Xu, J. Yue, S. Liu, J. Tu, F. Han, P. Liu, C. Wang, *ACS Energy Lett.* **2019**, *4*, 1073–1079; b) X. Yang, J. Luo, X. Sun, *Chem. Soc. Rev.* **2020**, *49*, 2140–2195.

[2] a) A. Manthiram, Y. Fu, S.-H. Chung, C. Zu, Y.-S. Su, *Chem. Rev.* **2014**, *114*, 11751–11787; b) H. Pan, Z. Cheng, P. He, H. Zhou, *Energy Fuels* **2020**, *34*, 11942–11961.

[3] S. Li, W. Zhang, J. Zheng, M. Lv, H. Song, L. Du, *Adv. Energy Mater.* **2021**, *11*, 2000779.

[4] a) N. Kamaya, K. Homma, Y. Yamakawa, M. Hirayama, R. Kanno, M. Yonemura, T. Kamiyama, Y. Kato, S. Hama, K. Kawamoto, A. Mitsui, *Nat. Mater.* **2011**, *10*, 682–686; b) Q. Zhang, D. Cao, Y. Ma, A. Natan, P. Aurora, H. Zhu, *Adv. Mater.* **2019**, *31*, 1901131.

[5] a) S. Rehman, M. Pope, S. Tao, E. McCalla, *Energy Environ. Sci.* **2022**, *15*, 1423–1460; b) T. A. Pascal, K. H. Wujcik, J. Velasco-Velez, C. Wu, A. A. Teran, M. Kapilashrami, J. Cabana, J. Guo, M. Salmeron, N. Balsara, D. Prendergast, *J. Phys. Chem. Lett.* **2014**, *5*, 1547–1551; c) K. H. Wujcik, T. A. Pascal, C. D. Pemmaraju, D. Devaux, W. C. Stolte, N. P. Balsara, D. Prendergast, *Adv. Energy Mater.* **2015**, *5*, 1500285; d) Z. Yang, Z. Zhu, J. Ma, D. Xiao, X. Kui, Y. Yao, R. Yu, X. Wei, L. Gu, Y.-S. Hu, H. Li, X. Zhang, *Adv. Energy Mater.* **2016**, *6*, 1600806; e) Q. Pang, X. Liang, C. Y. Kwok, L. F. Nazar, *Nat. Energy* **2016**, *1*, 16132; f) D. Zheng, G. Wang, D. Liu, J. Si, T. Ding, D. Qu, X. Yang, D. Qu, *Adv. Mater. Technol.* **2018**, *3*, 1700233.

[6] Y. Lin, J. Zheng, C. Wang, Y. Qi, *Nano Energy* **2020**, *75*, 104915.

[7] J. J. Zak, S. S. Kim, F. A. L. Laskowski, K. A. See, *J. Am. Chem. Soc.* **2022**, *144*, 10119–10132.

[8] W. Li, J. Liang, M. Li, K. R. Adair, X. Li, Y. Hu, Q. Xiao, R. Feng, R. Li, L. Zhang, S. Lu, H. Huang, S. Zhao, T.-K. Sham, X. Sun, *Chem. Mater.* **2020**, *32*, 7019–7027.

[9] Y.-T. Chen, M. A. T. Marple, D. H. S. Tan, S.-Y. Ham, B. Sayahpour, W.-K. Li, H. Yang, J. B. Lee, H. J. Hah, E. A. Wu, J.-M. Doux, J. Jang, P. Ridley, A. Cronk, G. Deysher, Z. Chen, Y. S. Meng, *J. Mater. Chem. A* **2022**, *10*, 7155–7164.

[10] B. Ding, J. Wang, Z. Fan, S. Chen, Q. Lin, X. Lu, H. Dou, A. Kumar Nanjundan, G. Yushin, X. Zhang, Y. Yamauchi, *Mater. Today* **2020**, *40*, 114–131.

[11] L. Xue, Y. Li, A. Hu, M. Zhou, W. Chen, T. Lei, Y. Yan, J. Huang, C. Yang, X. Wang, Y. Hu, J. Xiong, *Small Struct.* **2022**, *3*, 2100170.

[12] M. J. Gray, N. Kumar, R. O'Connor, M. Hoek, E. Sheridan, M. C. Doyle, M. L. Romanelli, G. B. Osterhoudt, Y. Wang, V. Plisson, S. Lei, R. Zhong, B. Rachmilowitz, H. Zhao, H. Kitadai, S. Shepard, L. M. Schoop, G. D. Gu, I. Zeljkovic, X. Ling, K. S. Burch, *Rev. Sci. Instrum.* **2020**, *91*, 073909.

[13] R. Fang, S. Zhao, Z. Sun, D.-W. Wang, H.-M. Cheng, F. Li, *Adv. Mater.* **2017**, *29*, 1606823.

[14] S. S. Zhang, *J. Power Sources* **2013**, *231*, 153–162.

[15] G. Wen, S. Rehman, T. G. Tranter, D. Ghosh, Z. Chen, J. T. Gostick, M. A. Pope, *Chem. Mater.* **2020**, *32*, 4518–4526.

[16] R. Fang, J. Xu, D.-W. Wang, *Energy Environ. Sci.* **2020**, *13*, 432–471.

[17] C. Xing, H. Chen, S. Qian, Z. Wu, A. Nizami, X. Li, S. Zhang, C. Lai, *Chem* **2022**, *8*, 1201–1230.

[18] a) D. Cao, Y. Zhang, A. M. Nolan, X. Sun, C. Liu, J. Sheng, Y. Mo, Y. Wang, H. Zhu, *Nano Lett.* **2020**, *20*, 1483–1490; b) H. Muramatsu, A. Hayashi, T. Ohtomo, S. Hama, M. Tatsumisago, *Solid State Ionics* **2011**, *182*, 116–119.

[19] Y.-X. Song, Y. Shi, J. Wan, S.-Y. Lang, X.-C. Hu, H.-J. Yan, B. Liu, Y.-G. Guo, R. Wen, L.-J. Wan, *Energy Environ. Sci.* **2019**, *12*, 2496–2506.

[20] Z. Sun, Y. Hu, F. Qin, N. Lv, B. Li, L. Jiang, Z. Zhang, F. Liu, *Sustainable Energy Fuels* **2021**, *5*, 5603–5614.

[21] C. Prehal, J.-M. von Mentlen, S. Drvarič Talian, A. Vizintin, R. Dominko, H. Amenitsch, L. Porcar, S. A. Freunberger, V. Wood, *Nat. Commun.* **2022**, *13*, 6326.

[22] Q. Yang, J. Lin, F. Li, J. Zhang, E. Zurek, G. Yang, *Phys. Rev. Mater.* **2021**, *5*, 059901.

[23] M. Aykol, S. Kim, V. I. Hegde, S. Kirklin, C. Wolverton, *Phys. Rev. Mater.* **2019**, *3*, 025402.

[24] a) A. R. Oganov, C. W. Glass, *J. Chem. Phys.* **2006**, *124*, 244704; b) Z. Falls, P. Avery, X. Wang, K. P. Hilleke, E. Zurek, *J. Phys. Chem. C* **2021**, *125*, 1601–1620; c) G. Cheng, X.-G. Gong, W.-J. Yin, *Nat. Commun.* **2022**, *13*, 1492; d) Y. Wang, J. Lv, L. Zhu, Y. Ma, *Phys. Rev. B* **2010**, *82*, 094116; e) V. F. Degtyareva, *Solid State Sci.* **2014**, *36*, 62–72.

[25] a) M. Mayo, K. J. Griffith, C. J. Pickard, A. J. Morris, *Chem. Mater.* **2016**, *28*, 2011–2021; b) B. Zhu, Z. Lu, C. J. Pickard, D. O. Scanlon, *APL Mater.* **2021**, *9*, 121111; c) L. Zhang, Y. Wang, J. Lv, Y. Ma, *Nat. Rev. Mater.* **2017**, *2*, 17005; d) A. R. Oganov, C. J. Pickard, Q. Zhu, R. J. Needs, *Nat. Rev. Mater.* **2019**, *4*, 331–348.

[26] Y. Wang, J. Lv, L. Zhu, Y. Ma, *Comput. Phys. Commun.* **2012**, *183*, 2063–2070.

[27] G. Luo, J. Zhao, B. Wang, *J. Renewable Sustainable Energy* **2012**, *4*, 063128.

[28] G. Yang, S. Shi, J. Yang, Y. Ma, *J. Mater. Chem. A* **2015**, *3*, 8865–8869.

[29] G. S. Pawley, R. P. Rinaldi, *Acta Crystallogr. Sect. B* **1972**, *28*, 3605–3609.

Manuscript received: February 15, 2023
Accepted manuscript online: March 14, 2023
Version of record online: April 12, 2023